ADVANCED NANOBIOMED RESEARCH Open Access
www.advnanobiomedres.com

Revealing Layer-Specific Ultrastructure and Nanomechanics of Fibrillar Collagen in Human Aorta via Atomic Force Microscopy Testing: Implications on Tissue Mechanics at Macroscopic Scale

Meisam Asgari, Neda Latifi, Francesco Giovanniello, Horacio D. Espinosa, and Marco Amabili*

Soft biological tissues are natural biomaterials with structures that have evolved to perform physiological functions, for example, conferring elasticity while preserving the mechanical integrity of arteries. Furthermore, the mechanical properties of the tissue extracellular matrix (ECM) significantly affect cell behavior and organ function. ECM mechanical properties are strongly affected by collagen ultrastructure, and perturbations in collagen networks can cause tissue mechanical failure. It is thus crucial to understand the ultrastructural mechanical properties of soft tissues. Herein, the ultrastructural and nanomechanical properties of arterial tissues are reported. Specifically, maps of aorta tissue stiffness in its three constitutive layers, namely tunica intima, media, and adventitia, are reported. Atomic force microscopy (AFM) with large and ultrasharp tips is used to explore tissue stiffness at two scales. Quasistatic tensile tests are further conducted to understand a potential correspondence between small-scale mechanical properties obtained via AFM indentation and macroscopic behavior of the tissue at low and large strains. Furthermore, gradients in stiffness across the various layers as well as deformation rate effects are investigated. It is envisioned that the established methodology serves as a tool to investigate the effect of ECM remodeling associated with vascular diseases such as aneurysms and arterial stiffening linked to hypertension.

1. Introduction

The elasticity of soft tissues has been a central research theme in biomedical applications as a tool for medical diagnosis. In pathological conditions or as a response to injury, the tissue ultrastructure might undergo substantial changes at the extracellular level. It is believed that disease or injury changes the local or overall elastic behavior of soft tissues. For instance, changes in the stiffness of a tissue at the macroscopic level might indicate the emergence of diseases such as liver fibrosis,[1] breast cancer,[2–4] and aortic disease.[5,6] In small scale, several cell behaviors such as cell morphology,[7] proliferation,[8,9] motility,[10] and the cell response to therapeutic agents[11] are significantly affected by changes in local and macroscopic elasticity of the tissue. Further, cancer cell migration causing metastasis to other organs is affected by the remodeling of the extracellular matrix (ECM) in the tumor area. Quantification of collagen structure and mechanics can thereby serve as an image-based biomarker to clinical specimen imaging trials.[12] The accurate structural and mechanical characterizations of soft tissues at macro- to nanoscale are thus central to understand how tissue biophysical behavior is related to its proper functionality. Fibrillar proteins such as collagen and elastin govern the stiffness and strength of biological tissues. Molecular proteins in human body, only a few nanometers in size, self-assemble to form fibrils with a

M. Asgari, F. Giovanniello, M. Amabili
Department of Mechanical Engineering
McGill University
817 Sherbrooke Street West, Montreal, QC H3A 0C3, Canada
E-mail: meisam.asgari@mail.mcgill.ca

The ORCID identification number(s) for the author(s) of this article can be found under https://doi.org/10.1002/anbr.202100159.

DOI: 10.1002/anbr.202100159

M. Asgari, H. D. Espinosa
Theoretical and Applied Mechanics Program
Northwestern University
2145 Sheridan Road, Evanston, IL 60208, USA

N. Latifi
Department of Mechanical and Industrial Engineering
University of Toronto
5 King's College Road, Toronto, ON M5S 3G8, Canada

hierarchical structure. The dispersion and entanglement of these fibrils contribute to the overall structure of the ECM. Thus, the tissue inherits its mechanical properties from the concentration, dispersion, and the mechanical properties of individual protein strands within ECM. Among several protein types, fibrillar collagen types I and III are the main load-bearing elements of most connective tissues forming ECM to support cells.[13]

A technique that has revolutionized the characterization of biological materials is atomic force microscopy (AFM), which simultaneously reveals morphological and mechanical properties.[14] In more recent years, AFM indentation has been used to extract mechanical properties of a variety of soft tissues.[15–18] In this technique, a few tens of micrometer long cantilever with a sharp conical or spherical tip scans the surface of the sample and creates a topographical image of the surface. In addition to imaging, the tip can poke into the surface of the sample with force sensitivity as low as pico-Newton to indent the surface up to a desired amount to quantify the local stiffness of the biomaterial. The deflection of the cantilever measured by the instrument is translated into the force between the tip and the sample via the cantilever stiffness. In one indentation cycle, the force versus cantilever deflection is recorded through approaching and retracting curves and the obtained data can be converted to the local mechanical stiffness using contact mechanics theories.[19] Moreover, the viscoelastic behavior of the hydrated tissue can be approximated from the displacement difference between the approaching and retracting curves. To obtain the bulk mechanical properties in soft tissues, the tip radius is selected to be large enough to indent a representative areal element of the material, which includes all surface features. When the radius of the tip is large, the indented area is large and thus the measurement represents an average over a volume that includes several biomaterial features. However, to obtain the properties of ultrastructural features, a sharp probe is utilized with a very spatial resolution that is commensurate with the dimension of the feature of interest (e.g., collagen fibril diameter).

Among biological tissues, the human aorta is of interest because it is the largest artery in the body. The aorta originates from the left ventricle of the heart and extends to the abdomen. This vessel is comprised of three layers: tunica intima (i.e., the innermost layer), media (i.e., the middle layer), and adventitia (the outer layer). The role of this vital tissue is to disseminate oxygenated blood to all sections of the human body. Along the aortic tissue, the descending thoracic aorta (located distal to the aortic arch) may experience bulging, called aneurysm.[20] The important role of this vessel highlights the significance of interrogating its biomechanical properties, which are deemed essential to the understanding of its physiology. More specifically, such investigations provide information, which is central to address problems in surgery as well as in medical device applications. Previous research demonstrates the change in mechanical properties of aortic tissue with age[21,22] or the presence of a disease; for instance, characterization of a chronic type A dissected aorta showed different mechanical properties in contrast to the healthy tissue.[23] Therefore, the mechanical properties are deemed as a fundamental indicator to assess the health condition of human aorta.

Various types of mechanical testing have been utilized to characterize the mechanical properties of human aortic tissue, the examples of which include uniaxial[21,24,25] and biaxial[26] tensile tests. Further, viscoelastic characterization of the full aorta under pulsatile pressure has been conducted using a mock circulatory loop.[22] Despite extensive studies on the macroscopic mechanical characterization of this tissue,[22,24,25,27,28] the literature is scarce on the micro- and nanostructural and mechanical characterization of the individual layers of human aorta. Of interest is the understanding of tissue stiffening due to ECM remodeling, mainly associated with changes in elastin and collagen content. Chemical modifications by age have been proven to change fibril elasticity.[29] It is thus imperative to interrogate structural and mechanical properties of the ECM constituents employing high-resolution imaging as well as multimodal characterization techniques. Brody et al.[30] used AFM to characterize topographic features of the native aortic valve endothelial basement membrane to provide a rational for the design of ECM with nanoscale features mimicking those of native aortic valve basement membrane. Peloquin et al.[31] used AFM indentation to measure the elastic modulus of the subendothelial matrix in bovine carotid arteries. Tracqui et al.[32] utilized AFM to obtain regional elastic properties of murine aortic plaques. Rezvani-Sharif et al.[33] also applied AFM to determine elastic moduli of aortic wall lamellae and plaque components. Berquand et al.[29] investigated the effect of age on the morphology and elasticity of mice aortic sections and found out that the stiffness of elastic fibers within mice aorta increases by age. In addition to the changes associated with the structure and mechanics of elastin and collagen fibers, they concluded that the tissue elasticity is affected at the molecular level. Jones et al.[34] presented a thorough ultrastructural quantification of collagen fibrils in abdominal aortic aneurysm to indicate the presence of heterotypic collagen fibrils with compromised D-spacing and increased curvature in the vascular tissue. Qiu et al.[35] applied AFM to investigate the changes in intrinsic vascular smooth muscle cell stiffness as a result of aging, to provide a mechanistic rationale for the application of pharmacological agents in the treatment of increased vascular stiffness. Sicard et al.[36] used AFM indentation with different tip sizes to investigate the elastic properties of human pulmonary small arteries and their sensitivity to the radius of the tip.

In this article, we report a systematic ultrastructural and nanomechanical experimental exploration on the layers of human thoracic aortic tissue to bridge the gap between understanding the ultrastructural and nanomechanical properties of human aorta and its overall tissue-level mechanical properties. Quasistatic uniaxial tensile tests on aortic strips are used to investigate the overall behavior of the tissue at the macroscopic level. We apply an extensive set of AFM experiments to visualize and quantify the ultrastructural and nanomechanical properties of this tissue at different layers down to the level of individual proteinaceous fibrils within ECM using high-resolution AFM imaging and force spectroscopy. In particular, we utilize AFM indentation testing on several sections of human thoracic aorta tissue at different layers to interrogate the structure and mechanics of each layer in the tissue and subtissue (i.e., tissue ultrastructure or single fibrils in the ECM) levels. The investigation lays a foundation for capturing ultrastructural and nanomechanical changes in tissue elastic properties concomitant with pathology and provides a robust tool to quantify the changes in the structure and cohesiveness of a soft tissue in response to disease or injury.

2. Results and Discussion

2.1. Ultrastructural Characterization of Aortic Layers

The quantity and quality of collagen fibrils in ECM play a crucial role in tissue biological processes.[37] We investigated the ultrastructural topography of single collagen fibrils within intima, media, and adventitia ECM by analyzing the fibrillar D-spacing (i.e., the sum of overlap and gap regions within the staggered arrangement of tropocollagen molecules forming a single collagen fibril[13]) as a metric of tropocollagen molecular packing within a single fibril[38–40] and fibrillar thickness. AFM topographical images were obtained from five healthy human donors as illustrated in **Figure 1**; donor I, male 47 years; donor II, male 60 years; donor III, female 51 years; donor IV, female 51 years; and donor V, female 50 years. **Figure 2** shows ultratopography AFM images of selected regions in longitudinal sections of intima, media, and adventitia. Similar to previous studies,[41] our results indicate the presence of fibrillar collagen with characteristic D-spacing pattern of 50–70 nm with either curved and straight geometric contours within intima, media, and adventitia (Figure 2a,b,d). AFM surface scans were produced over regions defined in transmission light microscopy integrated with the AFM system (Figure 1). Arrowheads point to large collagen fibers (green), large elastic fibers (yellow), anchoring single collagen fibrils (blue), and fine interconnecting collagen fibrils (white) within ECM at each layer and their attachment with other ECM components. At each layer, collagen fibers are formed by a combination of several collagen fibrils and are laterally entangled to give strength to the ECM of the tissue. Individual collagen fibrils within each fiber are connected through proteoglycans (formed by a sugar chain and a protein core) which are responsible for load transfer within the collagen fiber.[42] Each layer is further observed to contain fibrils with no evident D-spacing pattern (Figure 2a) or a D-spacing value below or above that of collagen type I fibrils. Similar to the results of the study by Dingemans et al.,[41] the thick fibrils without conspicuous D-spacing might be elastin. The fibrils with a D-spacing value below or above that of collagen type I fibrils (i.e., 64–67 nm) are presumably heterotypic collagen fibrils that contain both collagen types I and III molecules within the staggered structure of the fibril.[13,34] The copresence of collagen types I and III in human aorta has already been reported by Dingemans et al.[41] Figure 2b displays representative AFM surface scans with increasing scan resolution from left to right of adventitia, media, and intima from donor I. In this region of the tissue, which is different from the one shown in Figure 2a, the observed D-spacing periodicity corresponds to healthy tissue. As shown in Figure 2c, this pattern is found to be relatively consistent within each layer of healthy human aorta as the main structural feature of heterotypic fibrillar collagen in soft tissues.[13] Collagen D-spacing in intima of donor I (44.67 ± 6.52 nm) was found to be smaller than the D-spacing value in media (58.29 ± 7.37 nm) and adventitia (61.34 ± 7.01 nm), as shown in Figure 2e with no statistically significant differences between their mean values (one-way repeated measures ANOVA with post hoc Bonferroni's multiple comparison test, ($p < 0.0001$)). We also measured fibrillar collagen thickness in the three layers of the five donor tissues. For donor I, as shown in Figure 2e, collagen in intima (60.15 ± 8.67 nm) was smaller than the fibril thickness in media (64.39 ± 9.65 nm) and adventitia (81.43 ± 10.04 nm). The differences were statistically significant across the three layers for donor I ($p < 0.0001$) for intima versus adventitia and media versus adventitia. Human collagen in intima, media, and adventitia layers from the five healthy donors had an average fibril thickness of 94.46 ± 26.03 nm, 87.96 ± 18.20, and 91.76 ± 9.12, respectively, with no statistically significant differences in their mean values (Figure 2, one-way ANOVA, $p = 0.865$). Further, collagen in intima was found to have an average fibril D-spacing of 55.68 ± 6.21 nm, slightly smaller than that in media (58.21 ± 1.77 nm) and adventitia (57.59 ± 3.45 nm), yet again with no statistically significant differences in their mean values (Figure 2, one-way ANOVA, $p = 0.625$). Our results with regard to collagen fibril ultrastructural characteristics are consistent with those of healthy human samples as reported in a recent study on collagen fibril abnormalities in human abdominal aortic aneurysm (AAA) where significant changes in collagen geometry were found as a result of aneurysm.[34] Vascular tissues such as human aorta contain heterotypic load-bearing collagen fibrils of types I and III, stabilized by intramolecular cross-linking.[43] Slight variations in collagen thickness and D-spacing observed in the layers of five healthy aortas in our study could be the result of the copresence of type I and III collagen fibrils and their heterotypic fibrillogenesis.[13,37] Tonniges et al.[37] investigated the effect of discoidin domain collagen receptor 1 (DDR1) on the collagen content and ultrastructure of adventitia of DDR1 knock-out (KO) mice and found a small but statistically significant increase in the depth of D-spacing in DDR1 KO adventitia collagen fibrils in contrast to their wild-type littermates. However, similar to our results, they found no statistically significant difference in the length of D-spacing.

The overall mechanical behaviors of human aorta are observed to differ between the layers.[21,22,25] This dissimilarity of the behavior at the macroscale might originate from dissimilar distribution of collagen fibers (formed as a result of the cross-linking of several collagen fibrils) at different layers and their different entanglement patterns within each layer.[25] However, at the micro- to nanoscale, analysis of representative single collagen fibrils within ECM shows similar repetitive D-spacing and its variation along collagen fibrils. The mechanics of such fibrils is also consistent between the three layers, despite their potential dissimilar ratios of type I and type III collagen monomers within their heterotypic structure.[13]

AFM images from the three layers of the healthy tissue from donor I reveal collagen fibril unidirectional alignment within fibrillar bundles, also called fibril registration within ECM (Figure 2d). This unidirectional alignment also happens between collagen fibers forming a stiff network in a larger scale upon application of large strains on the tissue. As a consequence, the stiffness of the tissue at large strains increases. Furthermore, AFM visualization of healthy aorta from the five donors, at each layer, reveals a firmly knitted network of fibrils (Figure 2a,d). It is believed that such architecture and the alignment of the fibrils (Figure 2d) allows the expansion of the tissue while avoiding tissue overstretching at large strains.[43,44] A single collagen fibril within ECM is shown in Figure 2e, with the fibril thickness and D-spacing as the two metrics for

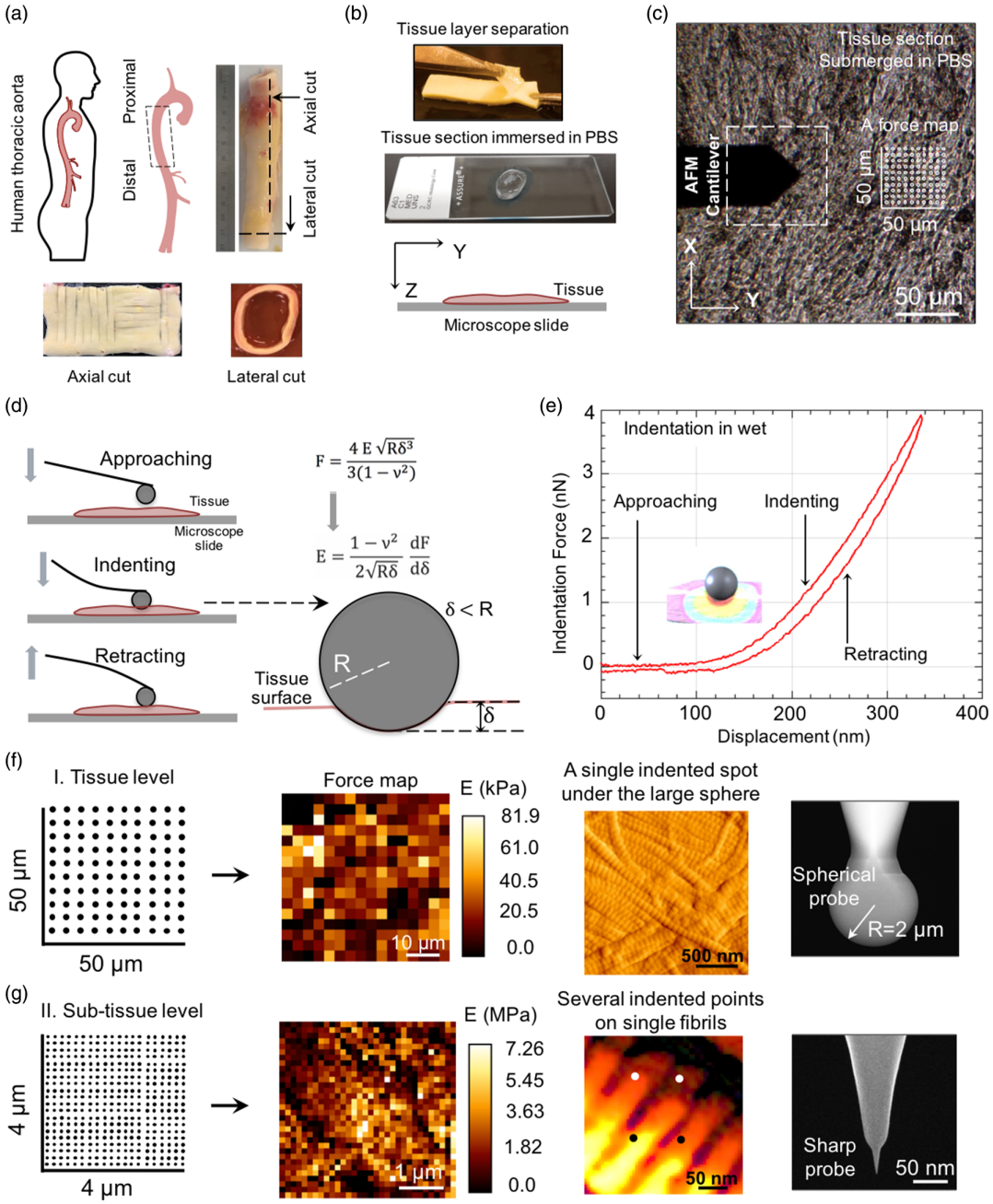

Figure 1. Nanomechanical characterization of human descending thoracic aorta using AFM; a) human thoracic aorta tissue is dissected. Axial and lateral cuts are made for in-plane and cross-sectional analysis; b) for in-plane analysis, the layers are separated and sectioned. Tissue sections of 20 μm thickness are cut from each of the separated layers as well as full-thickness cross sections of the tissue for AFM measurements. Tissue sections attached on microscope slide are tested while being immersed in PBS; c) optical image (top view) of the AFM probe on the tissue section submerged in PBS; a sample force map is shown in an area of 50 μm × 50 μm with indentation points; d) steps of the indentation of the tissue with a spherical tip with the tissue submerged in PBS. The AFM cantilever with a spherical probe is navigated over planar sections of intima, media and adventitia layers using an inverted bright-field microscope integrated with the AFM. Elastic modulus E is calculated by fitting the contact part of force–displacement (F–δ) curves using a standard Hertzian contact model. In the force curve, the interaction between the tip and sample is measured while the tip approaches and retracts from the surface of the sample. e) A representative curve showing the indentation cycle. Cantilever deflection is plotted against controlled deformation to obtain force–displacement (F–δ) curves at each point. Approaching and retracting curves provide information on the mechanical properties of the sample, as well as adhesion between the tip and sample. f,g) Tissue level (50 μm × 50 μm) and subtissue level (4 μm × 4 μm) force maps with several indentation points. Single indentation spots in each case are shown. Sample AFM contact mode images of a representative area of the ECM (for tissue level indentation) and a single collagen fibril (for subtissue level indentation) are shown. SEM images of the applied AFM probes (with 2 μm and 2 nm tip radii) for both levels of indentation are shown (Nanotools, USA).

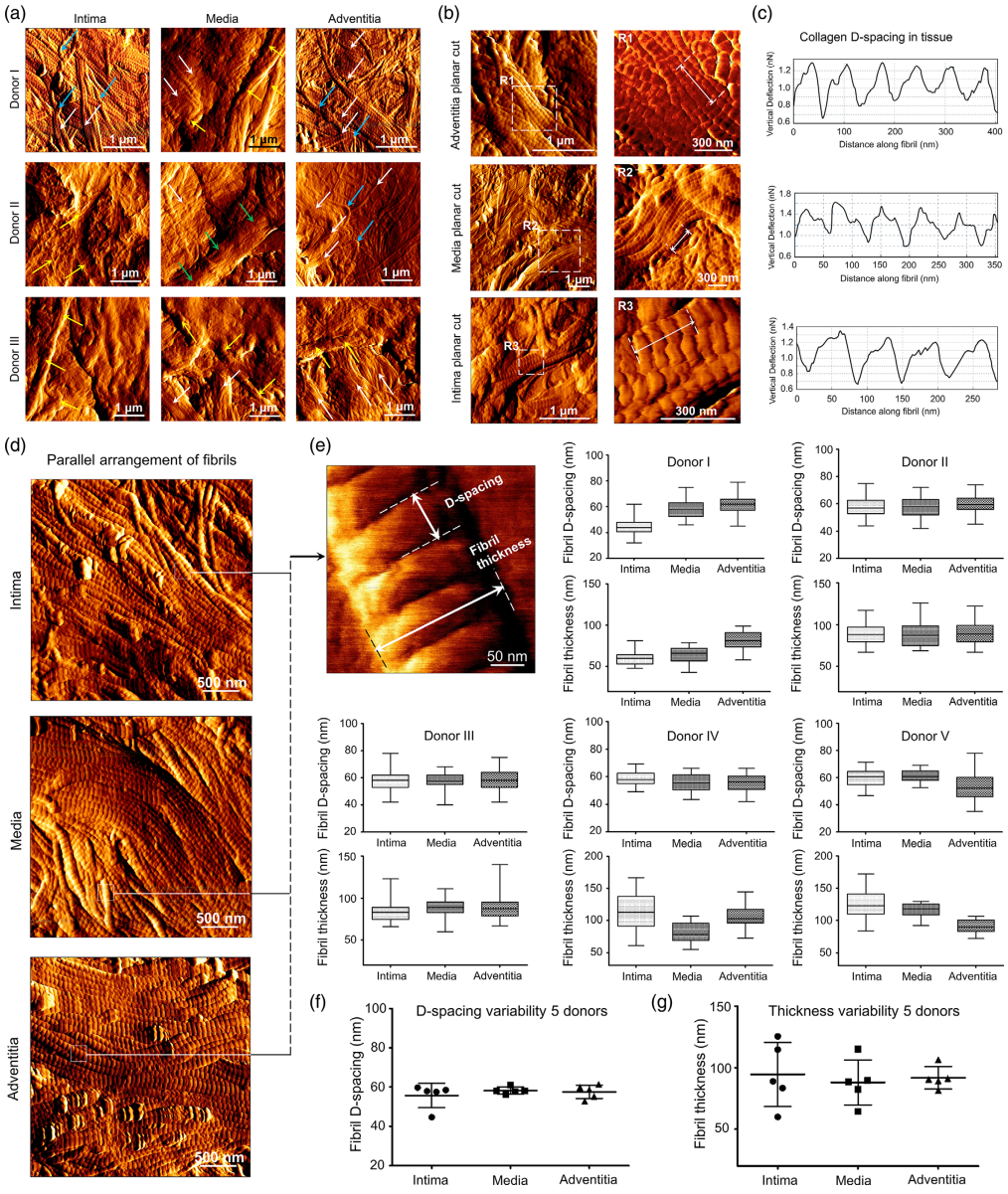

Figure 2. a) Ultra topography AFM images of selected regions in the layers of aorta in three human donors. AFM surface scans were produced from intima, media, and adventitia sections over regions defined in transmission light microscopy. AFM contact mode images were obtained in air using soft silicon nitride cantilevers with sharp probes. Arrowheads point to large collagen fibers (green), large elastic fibers (yellow), anchoring single collagen fibrils (blue), and fine interconnecting collagen fibrils (white) within ECM at each layer and their cross-linking with other ECM components. In some regions, fibrils with no evident D-spacing are observed copresent with normal collagen fibrils. b) Representative AFM surface scans are displayed with increasing scan resolution from left to right of adventitia, media, and intima to visualize D-spacing periodicity in the layers of healthy tissue from donor I. c) Image analysis by JPK software shows repetitive pattern (i.e., gap plus overlap regions) along collagen fibrils and its variation on representative single fibrils. d) Collagen fibril unidirectional alignment to form bundles in the three layers of the healthy tissue from donor I. Individual collagen fibrils shape laterally associated collagen bundles wherein the fibrillar D-spacing appears in register. e) A single collagen fibril within ECM with fibril thickness and D-spacing as two quantification metrics for ultrastructural analysis of heterotypic collagen fibril.[13,43] f,g) Respective collagen fibril D-spacing and thickness variability within ECM in five donors. No statistical significance is observed between the fibrils of the three layers. Longitudinal sections of intima, media and adventitia collagen fibrils in AFM images of aorta were utilized for thickness analysis. No statistically significant difference is observed between the D-spacing of the fibrils between the three layers of three healthy donors ($p = 0.625$). Fibril thickness variation between the three layers of the five donors is also observed to be statistically insignificant ($p = 0.865$). h,i) Fibril D-spacing and thickness variations within the layers in each of the three selected donors. D-spacing data for donor I indicated statistically significant difference between intima and media ($p < 0.0001$), and intima and adventitia ($p < 0.0001$). Also, D-spacing data for donor V showed statistically significant differences between intima and adventitia ($p = 0.0024$), and media and adventitia ($p = 0.001$), while the differences across the three layers were statistically insignificant for donors II ($p = 0.066$), III ($p = 0.691$), and IV ($p = 0.202$). Similar observations were made for fiber thickness where the differences were statistically significant across the three layers for donor I ($p < 0.0001$ for intima versus adventitia and media versus adventitia, one-way repeated measures ANOVA with post hoc Bonferroni's multiple comparison test.

microstructural analysis. Figure 2f,g shows respective collagen fibril D-spacing and thickness variability in intima, media, and adventitia in the five donors. No statistical significance is observed between the D-spacing of the fibrils across the three layers ($p = 0.625$). Fibril thickness variation between the five donors is also observed to be statistically insignificant ($p = 0.865$). The variation of these metrics between the layers in each of the five donors also shows no statistical significance (Figure 2e).

2.2. Mechanical Characterization of Aorta at Tissue and Subtissue Levels

The first step to understand the mechanics of a tissue is to characterize the mechanical and structural properties of its constituent. A soft tissue consists of ECM and cells, which interact with each other. One of the most abundant components in ECM is collagen. This protein is the most prominent factor in tissue stiffness and thus its mechanics has been thoroughly investigated.[13] Another ECM component that contributes to the mechanics of the tissue is elastin, which increases the compliance of the tissue and thus makes it easier to undergo larger elastic deformations.[22] Unlike collagen, elastin fibrils do not show D-banding periodicity and are merely responsible for elasticity of the tissue. Similar to collagen, elastin forms fibrous networks. Collagen and elastin networks intertwine within ECM while being structurally independent.[25] The synergic entanglement of these two networks is vital to provide arteries with necessary mechanical properties to sustain the blood pressure and to regulate the blood flow.[25]

Tissue sections of intima, media, and adventitia from five healthy donors were mechanically tested at two scales using different AFM probes: spherical probes of either 4 or 10 μm diameter and sharp probes with 4–10 nm tip diameter. The aim was to compare stiffness of the tissue at ECM structural and ultrastructural scales, respectively. While spherical probes with large diameters were utilized to obtain properties of each layer at the tissue level, the sharp probes were selected to specifically indent single collagen fibrils in ECM. The two different measurements thereby allowed the comparison of such properties with those obtained at the macroscale using conventional methods. Stiffness measurements with the two probe diameters, at each of the three layers, reveal a dependency of such properties to the size of the indented region. As a result of the pico-Newton force resolution of AFM and its lateral resolution (which facilitates up to several indentations in a few micrometers squared region), maps of mechanical properties of the tissue were obtained in a selected region. Using the mapping module, multiple single indentation measurements are integrated in a squared area to create a stiffness map, which provides a visual representation of stiffness in the selected area (see **Figure 3** and **4**).

Using a large tip radius in a squared region (on the order of tens of micron) makes it possible to map the bulk stiffness of the tissue in that region (Figure 3a–c), whereas using a sharp probe in a small region (on the order of a few microns) provides the stiffness map of the tissue ultrastructural constituents (Figure 4a–c). Further, increasing the number of points within each map (while considering the necessary distance of the adjacent indented points to avoid overlapping of the indented points) increases the spatial resolution of the stiffness map (Figure 4a–c). Tissue stiffness in the three layers of aorta was measured for five donors. Stiffness maps in large (Figure 3a–c) and small (Figure 4a–c) scales show that the distribution of elastic modulus across individual layers of aorta as well as among five donors varies by location, which is evidence for tissue heterogeneity at two scales. The level of the stiffness values within large (kPa) and small (MPa) maps, however, remains consistent between the five donors, as shown in the histogram distributions in Figure 3 and 4a–c. As shown in Figure 3f, there was no statistically significant differences between the mean stiffness values in intima (24.04 ± 13.97 kPa), media (22.18 ± 5.54 kPa), and adventitia (22.54 ± 3.35 kPa) (one-way ANOVA, $p = 0.941$). Our obtained stiffness values are in well agreement with those reported in recent AFM characterization studies on human aortic tissue.[33,36]

Ultrastructural elastic modulus E of human descending thoracic aorta was also obtained via wet indentation with a sharp probe from the five donors. It should be noted that the tissue does not present an initial prestretch. Small scan areas were mapped to obtain ultrastructural details of the tissue including single collagen fibrils within ECM. The values of elastic modulus were measured over 8×8 (mesh I), 16×16 (mesh II) and 32×32 (mesh III) points in five 4 μm $\times$ 4 μm zones (each zone from a separate donor) in planar sections in each of the three layers. Single collagen fibrils and collagen bundles were observed in each image (Figure 2a–d and 4). Figure 4a–c shows AFM images of some representative probed zones and the distribution of sample height and elastic modulus E within 4 μm $\times$ 4 μm areas in color-coded maps. Results indicate that the level of elastic moduli increases with the number of points in the mesh, with the elastic modulus converging to that of single collagen fibrils. In each case, histograms of fibril stiffness from mesh III are plotted on the right column. Results from the five donors in mesh I, II, and III in separate layers are also shown in Figure 4d. The elastic modulus increases by increasing the number of mesh points within the same area. The measurements show that collagen stiffness in intima (7.31 ± 3.5 MPa) is slightly larger than the one in media (4.38 ± 1.86 MPa) and adventitia (6.42 ± 4.20 MPa), as shown in Figure 4d (mesh 32×32) with no statistically significant differences between their mean values (one-way ANOVA, $p = 0.390$). These results are consistent with studies on native and synthesized collagen fibrils in wet state.[13]

2.3. Correspondence Between Small-Scale Characterizations (Tissue and Sub-Tissue Scales) and Macroscale Characterizations

Figure 5 displays graphs of uniaxial quasistatic tensile tests for rectangular strips of media cut from donors I, IV, and V in both longitudinal and circumferential directions bearing in mind the anisotropy of the tissue. In each case, the first Piola–Kirchhoff stress (i.e., engineering stress) is plotted against the engineering strain. As Figure 5 demonstrates, stress–strain curves are highly nonlinear. The tissue can be modeled with a hyperelastic material model in which the stiffness progressively increases with the

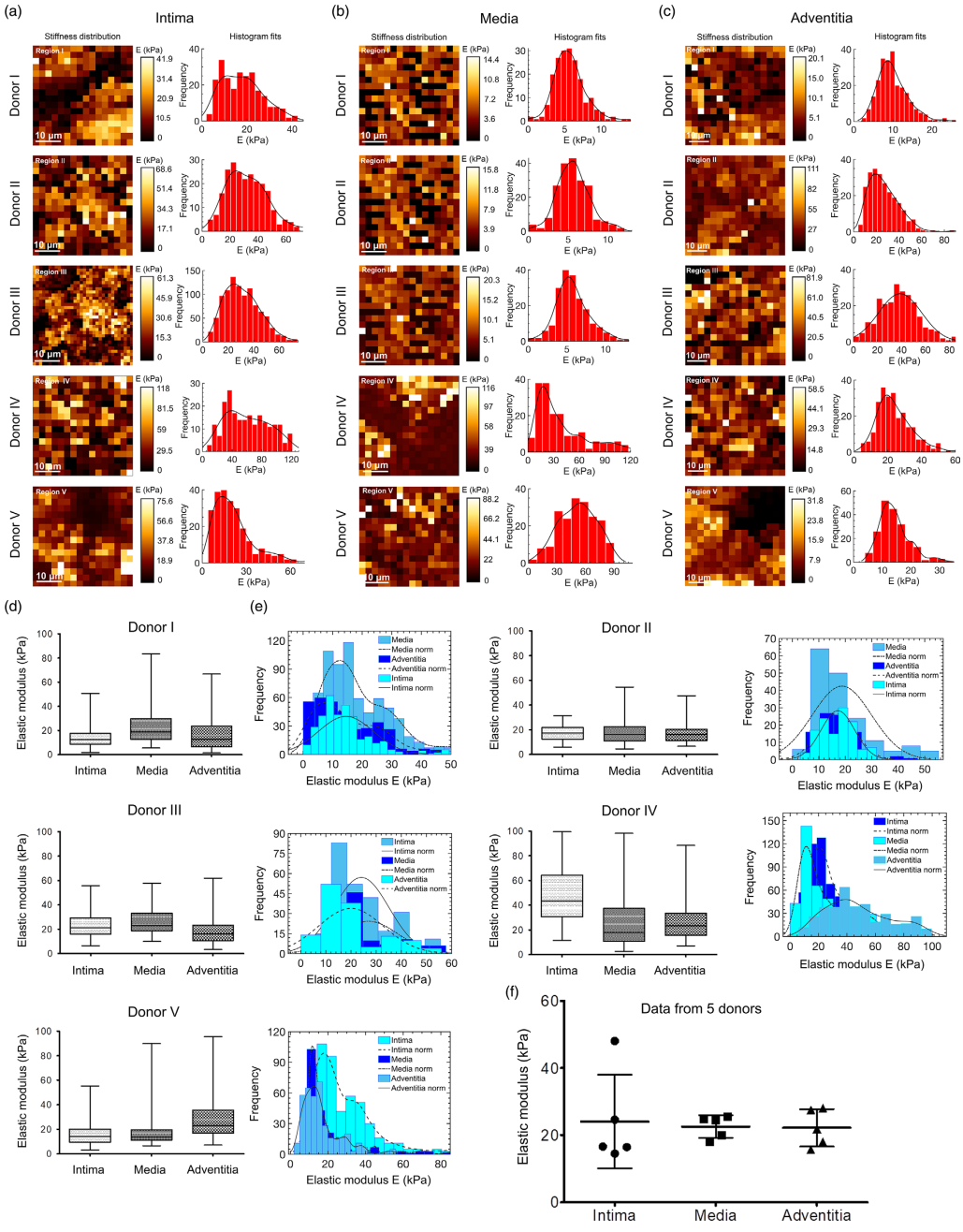

Figure 3. Force mapping and indentation modulus of human descending thoracic aorta obtained in wet indentation with 2 and 5 μm radius spherical probes, respectively: samples from five healthy human donors were characterized; a–c) representative force maps from 50 μm × 50 μm regions in intima, media, and adventitia in the five donor samples, with their corresponding elastic modulus distribution histograms. Each pixel in the force maps represents a force curve. d) Indentation results in the three layers of the five donors using a 5 μm radius tip, represented in box-and-whisker plots. In each case, 4 × 4 points in at least ten different 30 μm × 30 μm regions in each of the three layers of human aorta were indented. Statistically significant difference is observed between the stiffness values across the three layers for donors I and III ($p < 0.0001$). Bonferroni's multiple comparison test revealed significant difference in elastic moduli between intima and media ($p < 0.0001$), and media and adventitia ($p < 0.0001$) for donor I, and between intima and adventitia ($p = 0.0009$), and media and adventitia ($p < 0.0001$) for donor III. e) *E* values of intima, media, and adventitia (in donor I, II, and III, respectively), assembled in a histogram and fitted with probability density estimates (black traces on the graphs) to determine the most probable value of the elastic modulus of the tissue in each case. On each box, the central black line is the median, the edges of the box are the first and third quartiles, and the whiskers extend to the minimum and maximum data points considered not to be outliers. f) Indentation results of the five donors' layer by layer in one graph. No statistically significant difference is observed between the stiffness of the layers in the five healthy donors ($p = 0.941$).

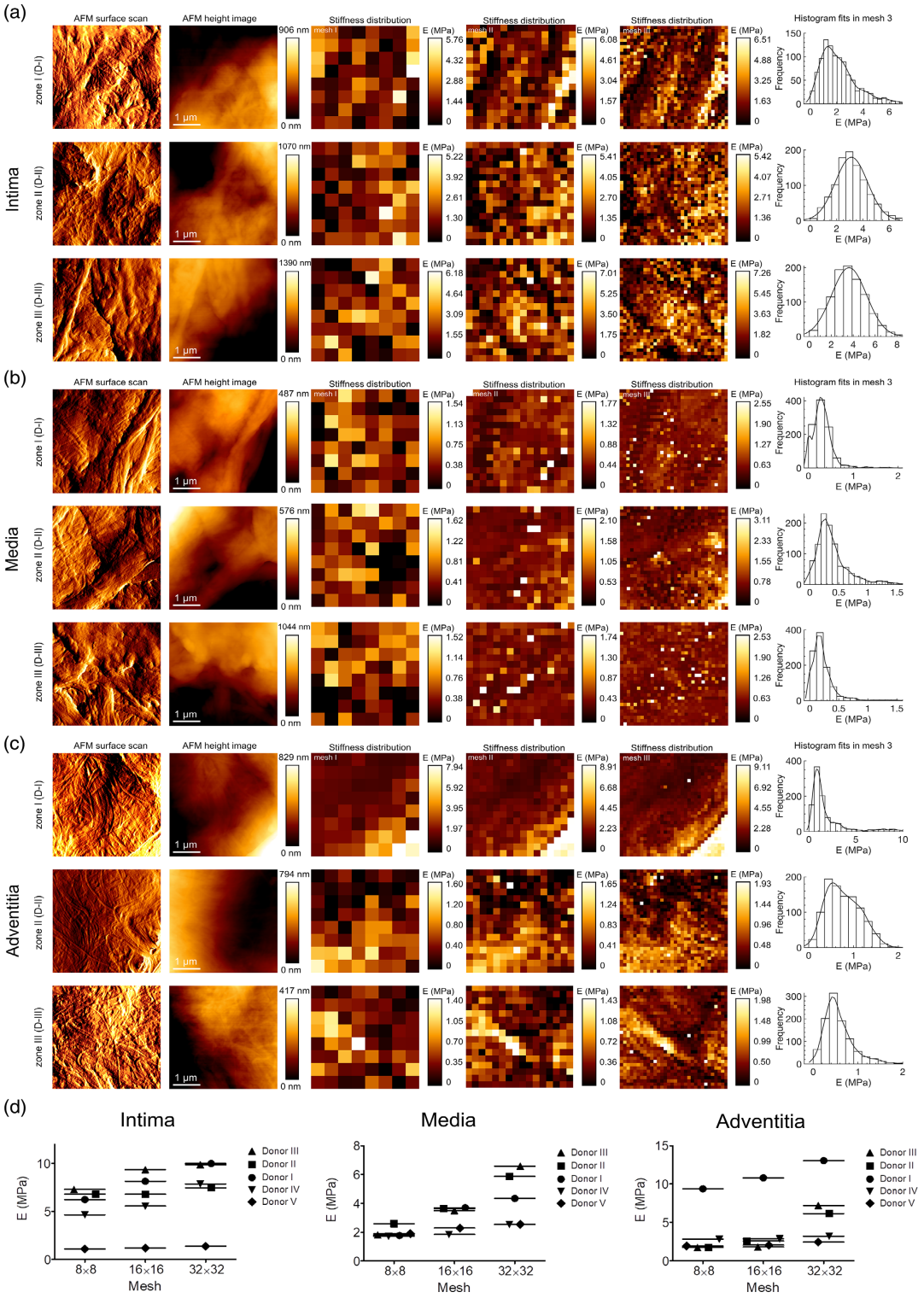

Figure 4. a–c) Ultrastructural elastic modulus *E* of human descending thoracic aorta obtained in wet indentation with a sharp probe from three selected donors. Reduced scan areas were selected to obtain the structural details of the tissue including single collagen fibrils within ECM. The values of elastic modulus were measured over 8 × 8 (mesh I), 16 × 16 (mesh II), and 32 × 32 (mesh III) points in three 4 μm × 4 μm zones in planar sections in each of the three layers (intima, media, and adventitia). Single collagen fibrils and collagen bundles are observed in each image. AFM images of some representative probed zones and the distribution of sample height and elastic modulus E within 4 μm × 4 μm areas are shown in color-coded maps. Results indicate that the range of elastic moduli increases with the number of points, converging to the one for single collagen fibrils. Distribution of fibril stiffness from mesh III is plotted in the histograms. d) Results from the five donors in mesh I, II, and III in separate layers. The elastic modulus increases by increasing the number of mesh points within the same area.

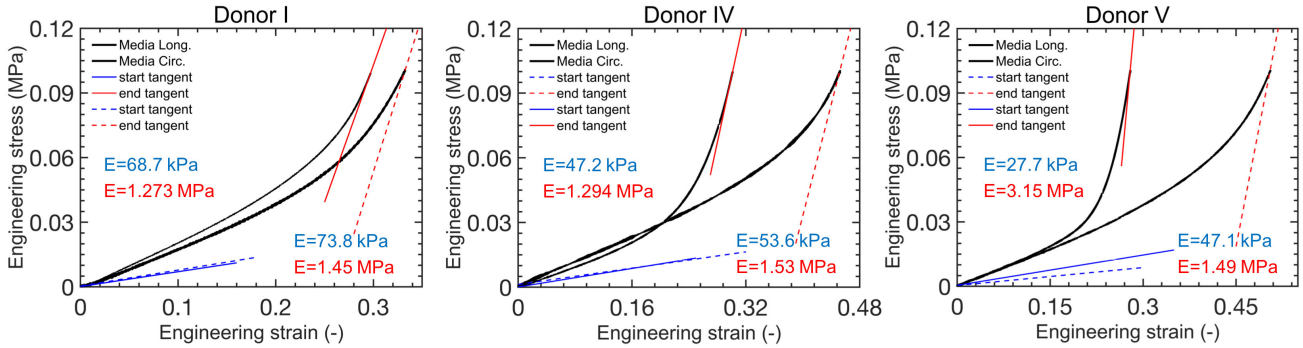

Figure 5. Uniaxial tensile testing results on longitudinal and circumferential strips cut from media of donor I, IV, and V in the elastic regime. First Piola–Kirchhoff stress (i.e., engineering stress) is plotted against engineering strain. The slopes of the tangent lines to each of the curves at the very beginning (blue) and at the end (red) show a qualitative correspondence with the indentation with large sphere and that with a sharp probe, respectively.

strain, due to the original crimped configuration of the collagen fibers.[25] The slopes of the tangent lines to the curves at the beginning and at the end show a qualitative value for the estimation of elasticity of the tissue before and after collagen uncrimping. We observe a qualitative correspondence between the values of elastic modulus obtained by indentation using a sharp tip (Figure 4), which are in megapascal regime, with the maximum slope of the stress–strain curves observed in Figure 5. On the other hand, the values of the elastic modulus obtained through AFM indentation with a spherical probe shows an approximate correspondence with the slope of the stress–strain curves at the outset of uniaxial loading. It should be noted that the exact outset of the stress–strain curves in the tensile tests introduces some challenges due to the residual stresses in the specimen and the initial preconditioning. This complication might introduce some difficulty in appraising the accurate stiffness value at very small strains from tensile test.

It is known that the stiffness of a single collagen fibril is within the gigapascals (GPa) and megapascals (MPa) ranges in dehydrated and hydrated states, respectively.[13,45] These hierarchical fibrillar protein structures contribute to the bulk mechanics of the tissue through their cross-linking, to form fibers, their orientation, and volume fraction, which define the organization and assembly of the tissue ECM.[21,25] Individual collagen fibrils (with 100–500 nm thickness, a D-banding periodicity of ≈67 nm and length of up to a few microns) merge and form crimping collagen fibers with tens of micron length and thickness.[13,25] Random distribution of such fibers within ECM explains the low stiffness of the tissue at small strains, mainly on the order of kilopascal.[46] Upon applying large strains, these collagen fibers uncrimp and align to form a stiff network. The stiffness of the tissue at large strains is thus rapidly increased up to that of collagen. This explains the nonlinearity of the stress–strain curves (also called J-shaped curves)[47,48] observed in tensile tests on several tissues such as longitudinal and circumferential strips of human thoracic aorta,[21,22,24,25] with the outset of deformation requiring a relatively low applied stress, while much higher stresses needed to impose larger strains.[47] Upon releasing the applied load at large strains, the tissue minimizes the deformation and returns to its original state. This high capacity of soft biological tissues to undergo large elastic strain is in part due to their ability to reorganize the orientation and arrangement of collagen fibers within the ECM (Figure 2a,d).[25] The flexibility of aorta at low strains causes the tissue to easily expand up to a certain extent. The stiffening part, however, prevents the overstretching of the tissue.[43,44] This highlights the significance of tissue mechanical characterization at small and large strain levels. At the micro- and nanoscale, this can be achieved by indentation of the tissue with large and sharp probes.[45] The former provides the stiffness of the ECM with a representative volume of the tissue involving a network of fibers, whereas the latter resolves the stiffness of single protein fibrils within the ECM.[45] While the former yields the mechanical properties of the tissue as a combination of those of collagen, elastic fibers (such as elastin), and glycosaminoglycans (GAGs), the latter differentiates those of individual constituents. As the AFM images of selected regions illustrate, the majority of the ECM in different aorta layers include collagen with apparent D-banding periodicity. Thus, the elastic moduli measured with sharp tip, in the MPa range (Figure 4), are analogous to the high-strain stiffness values observed in macroscopic tensile tests. Similarly, the elastic modulus measured with a large diameter tip, in the kilopascal (kPa) range (Figure 3), correlates with the low-strain stiffness region in macroscopic tensile tests. Both stiffness regimes are central to be considered in tissue engineering. Ignoring the low-strain stiffness regime might result in culturing engineered tissues with unnecessarily large stiffness values that are eventually unable to support organ flexibility.[47] Additionally, disregarding the large-strain stiffness regime when culturing a tissue would result in a weak mechanical response unable to resist damage at large strains.[47]

2.4. Gradients at Interfaces

We performed elastic modulus characterization along cross-sectional lines of complete aortas from the inner layer toward the outer layer. The aim was to explore the variation and continuity of stiffness values along the radial direction. As **Figure 6** illustrates, stiffness values from each layer were found to change while moving toward its adjacent layer(s) with a gradient across transition zones. The two transition zones are located around the membrane elastic interna and externa, which separate media

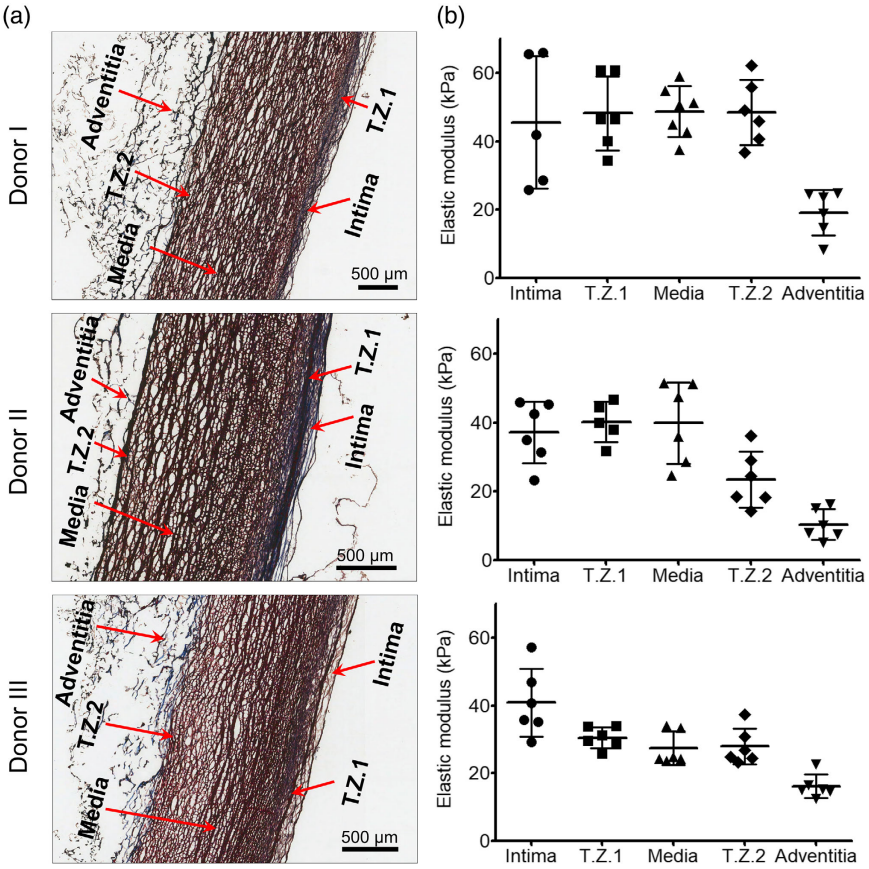

Figure 6. a) Representative images of Masson trichrome stained cross sections of the three aorta samples showing collagen fibers in intima, media, and adventitia and the transition zones from each layer to its adjacent layer(s); b) the elastic moduli across the section for three donors. The elastic modulus changes smoothly from each layer to the next layer with a smooth gradient in elastic modulus values. One-way repeated measures ANOVA with post hoc Bonferroni's multiple comparison test showed statistically significant differences in the elastic modulus of the layers and transition zones ($p \leq 0.0002$) for each donor. Bonferroni's multiple comparison test revealed statistically significant differences between the adventitia and each of the other two layers and two transition zones.

from its two adjacent layers (Figure 6a). Histology substantiates the presence of vascular smooth muscle in these transition zones. However, muscular fibers in such regions are thinner and less elongated than those in the central portion of media. The variations of fiber alignment and density might follow different trends at dissimilar layers, leading to diverse dependence of local structural and mechanical properties on location. As observed in Figure 6b, the properties typically change gradually from one layer to its adjacent layer(s). A more pronounced elastic modulus change was measured in transition zone 2, media–adventitia, for donor I, and in transition zone 1, intima–media, for donor III. These findings are consistent with the fact that Nature presents an extensive set of living organisms, which exhibit gradients in materials with limited structural and geometrical variables. Natural gradients in biological tissues such as bone or arteries are basically associated with the changes in either compositional or structural characteristics that include dimension, orientation, distribution, and arrangement of structural building blocks (mainly collagen) within ECM.[49,50] Interfacial regions are also central to maintain structural integrity of the biological tissue and to sustain its specific function.[50] Thus, it is advantageous to encompass gradual transitions of material properties to alleviate the mismatch between the properties of dissimilar regions as a natural design motif at such interfaces.[51] This leads to programmed response of the tissue to internal and external stimuli which prevents organ's failure. Damage of the tissue at the interfaces between layers in the case of aortic tissue may cause aneurysm (i.e., segmental weakening of the aorta) or acute aortic dissection that could be fatal.

The existence of site-specific structural and mechanical properties within biological materials caused by variations in factors such as geometry, microstructure, morphology, and composition is an important overarching feature of such materials that gives rise to structural and material functional gradients within these materials.[49] Functional gradients featuring in the microstructure of biological materials such as biological tissues and organs have exceptional implications on the resistance of such materials to failure and rupture in response to large deformations or mechanical loads.[49,51] One of the main sources of such properties is the gradual change in the mechanical properties within each biological organ as well as between the adjacent constituting parts of that organ.[52,53] The existence of such gradients within

the microstructure of biological tissues may originate from several sources such as the orientation and alignment of microstructural elements of the tissue (i.e., collagen, elastin, and gags) and their density and the degree of their crosslinking, as well as the chemical components of the material.[25] Dissimilar arrangement and density of stiff elements within the tissue introduce anisotropy and heterogeneity within the sections, which eventually causes the emergence of gradual changes in the mechanical properties within ECM.[52,53] At the interfaces between dissimilar regions or layers of the same organ, the main role of these functional gradients, particularly the gradients in the change of mechanical properties, is to smoothen the innate mismatch between material properties at the two regions, precluding failure or rupture of the organ at those interfaces.[51] Structural functional gradients in a layered tissue can be described in terms of spatial changes in ECM ingredients (stiff elements such as collagen fibers and elastic elements such as elastin) and their arrangement across the entire tissue or within a certain zone such as the interface regions[50] where dissimilar layers meet. Such regions denote the extremes in property changes.

2.5. Viscoelastic Behavior of Aortic Tissue: Rate-Dependent Mechanical Properties

Most biological materials exhibit loading-rate-dependent mechanical response to applied force (i.e., a strong elastic response at large deformation speeds and a strong viscous behavior at low deformation speeds).[13,52,54] In particular, the mechanical properties of soft tissues are contingent upon the applied loading rate.[52] The mechanical properties of biological tissues exhibit a nonlinear relationship with loading rate due to the viscoelastic nature of the ECM. Viscoelastic materials are characterized through time-dependent tests in which the deformation is applied as a function of time to measure the required forces or

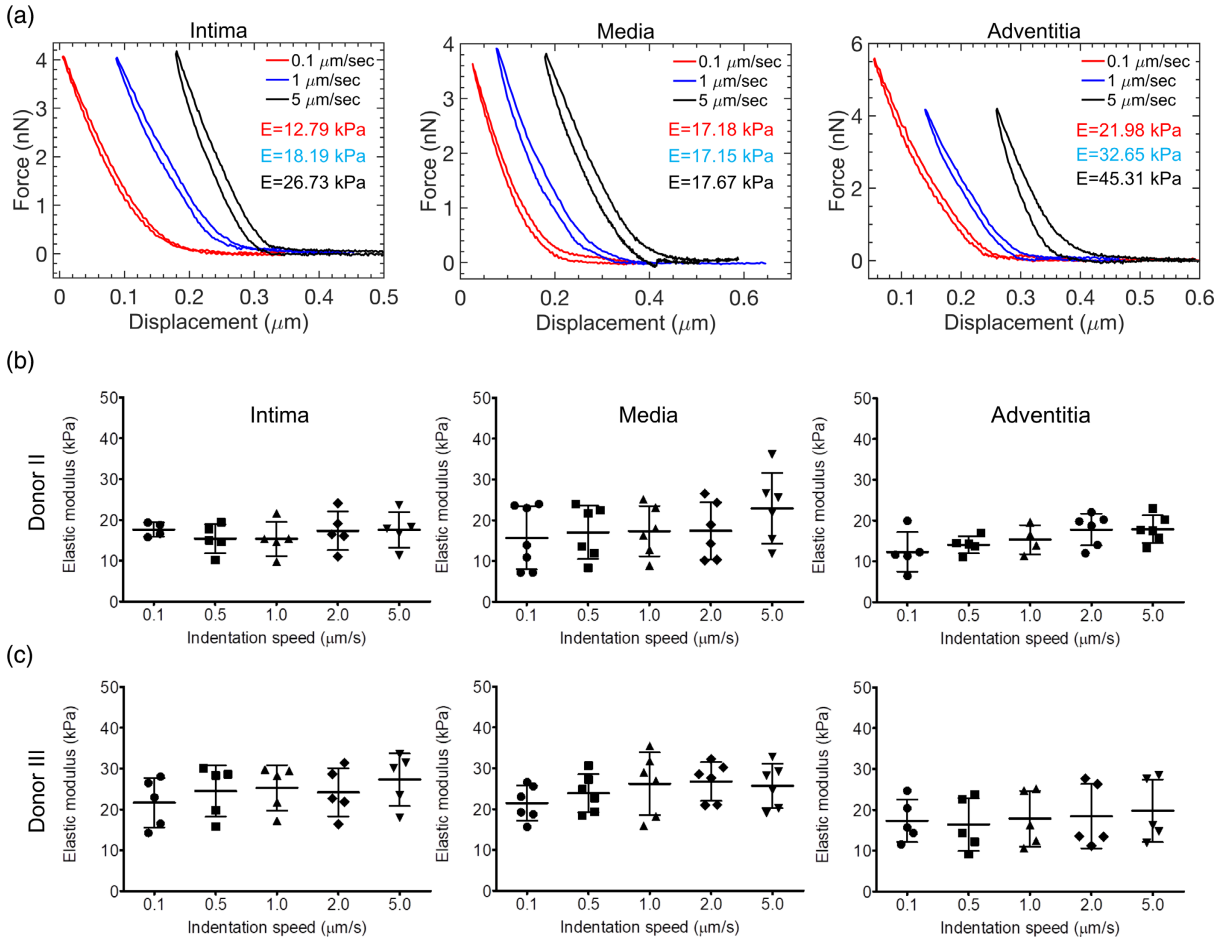

Figure 7. a) Selected examples of indentation curves from intima, media and adventitia of donor II obtained at speeds of 0.1 μm s^{-1} (red), 1 μm s^{-1} (blue), and 5 μm s^{-1} (black) resulting from a selected net of indentation points in hydrated state. The indentation frequency was changed to observe the qualitative viscoelastic behavior of the tissue. In this set, the values of the elastic modulus *E* in intima and adventitia slightly change by increasing the indentation speed, due to tissue viscoelastic effects. The force-indentation curves exhibit negligible adhesion between the tip and the samples. b,c) Indentation results from intima, media, and adventitia in samples from donor II (male) and donor III (female) in wet state at different indentation rates starting from 0.1 μm s^{-1} (quasistatic) to 5 μm s^{-1}. Variation of tissue stiffness by the speed of indentation is observed. No statistically significant differences were observed for the elastic moduli of each layer across different indentation rates ($p > 0.05$, one-way repeated measures ANOVA with post hoc Bonferroni's multiple comparison test).

vice versa. As such, obtaining the mechanical properties of soft tissues, in particular in wet state without specifying the loading rate, could be misleading. Hence, to conduct mechanical testing on soft tissues, time dependency of the applied force/displacement needs to be accounted for. At macroscopic scale, dynamic mechanical analysis (DMA) is commonly applied to evaluate the response of the material at different deformation rates, which yields the storage and loss moduli.[24] Such tests yield larger stiffness for the response of biological materials by increasing the deformation rate. At small scale, changing the speed of the AFM cantilever, and thus the speed of pushing the spherical probe into the surface of the sample, reveals viscoelastic effects.[13,52] Here, we applied this method to compare the mechanical behavior of aorta tissue at different indentation speeds ranging from 0.1 $\mu m\,s^{-1}$ (i.e., quasistatic) to 5 $\mu m\,s^{-1}$. We performed these tests on two healthy aortas, one male (donor II) and one female (donor III) (see **Figure 7**). As illustrated in Figure 7a–c, the value of stiffness at each layer shows a mild rate dependency within investigated deformation speeds. Our tissue-level mechanical characterization revealed that the mean stiffness of the aorta tissue slightly increases when the indentation rate varies from 0.1 to 5 $\mu m\,s^{-1}$ (Figure 7d–e), although the differences fall within statistical variations (Figure 7d–e). Detailed layer-specific viscoelasticity analysis of human aorta, using relaxation-based AFM indentation, is left for future investigations.

3. Conclusion

Human aorta presents a well-defined structure and a complex mechanical behavior. This is in part due to its anisotropy and heterogeneity, with an almost unpredictable distribution of its ECM components such as collagen fibrils. Moreover, the interaction of ECM and cells gives rise to additional complexity. Structural and mechanical characterizations of human thoracic aortic ECM, at micro- and nanoscales, have been scarce. This work aimed to improve the understanding of how collagen fibrils contribute to bulk mechanical properties of the aortic tissue by bridging the gap between small-scale and macroscopic properties of the tissue. This knowledge is central to improve the prediction of the tissue bulk material properties, e.g., using homogenization techniques, based on the mechanical properties of ECM constituents. Here, an extensive investigation of micro- and nanoscale structural and mechanical properties of five healthy human aortas was conducted. Each layer was individually studied; in particular, ultrastructural and nanomechanical properties of the layers were compared with their tissue-level counterparts.

Biological materials, including hard and soft tissues, demonstrate an array of hierarchical arrangements across length scales that are deemed essential to mechanical properties emerging from tissue building blocks.[55] Such hierarchical arrangements evolved to reach overall properties that confer arteries with functional elasticity while preserving mechanical integrity. In this work we show that while the mechanical stiffness of single collagen fibrils in the layers of human aorta is on the order of a few megapascals, the hierarchical entanglements of such fibrils with other ECM components lead to tissue-level mechanical stiffness of the order of kilopascals. Such tissue stiffness enables necessary deformations while smoothening the highly pulsatile nature of the blood flow in the aorta (Windkessel effect).[22] Therefore, the microstructural and nanomechanical quantification methodology presented in this study can serve as protocols to investigate ultrastructural changes resulting from various diseases, e.g., atherosclerosis, wherein fibrillar geometry and stiffness changes within ECM may help predict plaque rupture.

4. Experimental Section

Tissue Dissection and Layering: Descending thoracic aortas from five heart-beating male and female donors, with 47, 50, 51, 51, and 60 years old ages, were explanted during organ donation for transplants and obtained through a research agreement with Transplant Quebec approved by the Ethics committee at McGill University (IRB study number A05-M15-17 A). The aortas were retained in Belzer UW organ preservation solution at 4 °C prior to sample preparation. As shown in Figure 1a,b, tissue preparation for testing included: 1) removal of the external connective tissue and bifurcating arterial branches; 2) excising longitudinally the aorta on the posterior part; 3) cutting strips; and 4) separating the three layers. The tissue was opened up with a longitudinal cut along the posterior part, between the bifurcating intercostal arteries in order for the bifurcating holes to appear along the cut edges and the anterior portion of the aortic tissue to be in the central part (see Figure 1a). Rectangular pieces were cut from the opened-up tissue, to separate the three layers—intima, media, and adventitia. The layer separation needs attentive craftsmanship to avoid tissue damage. The accuracy of the layer separation was examined using confocal microscopy of stained tissue prepared for histology (see Amabili et al.[25] for more details). In addition to the layered sections, intact circumferential ring sections (Figure1a) were cut and sectioned for the analysis of cross-sectional transition zones (Figure 5).

Tissue Preparation for AFM Testing: Specimens of human thoracic aortic tissue were embedded using a mold to better preserve their orientation. Optimal cutting temperature (OCT) compound was chosen as the embedding medium. At the end of the procedure, the embedded sample is frozen and ready to be cut. The embedded blocks were trimmed. A microtome (Leica RM 2165) was applied to perform frozen sectioning on tissue samples from intima, media, and adventitia to obtain rectangular planar cuts with 20 μm thickness size and minimum surface roughness. The in-plane sections were taken about the middle of each separated layer. The sections were instantly attached to microscope glass slides with tissue axis directions being marked. The slides were then stored at −80 °C.

Trichrome Staining: Cross section of the human aorta was stained employing Masson trichrome via using the automatic stainer Leica ST5020. Coverslips were applied using the Leica CV5030 automated cover slipper and images were taken using a Leica Aperio AT Turbo digital pathology scanner.

AFM: A JPK atomic force microscope model Nano-wizard 4 (Bruker Nano, Berlin, Germany) mounted onto the stage of an inverted epifluorescence Zeiss Axiovert 200M microscope (Carl Zeiss Microscopy, Göttingen, Germany) was used for imaging and mechanical characterization of planar and transversal sections of human descending thoracic aortic layers. A microtome (Leica RM 2165) was applied to perform frozen sectioning on tissue samples from intima, media, and adventitia to obtain rectangular planar cuts with 20 μm thickness size. The sections were instantly attached to microscope glass slides with tissue axis directions being marked. The maximum lateral scans focused on regions of the area of 50 μm × 50 μm size. Scanning rate was set to 1 Hz. To characterize the nanostructure of tissue at each layer, AFM images were captured in contact mode and at a resolution of 1024 × 1024 pixels. Tissue sections (three biological replicates, each from separate donors, with three layers and two cross sections, three slides per case, and two replicate sections per region on each slide) were imaged and mechanically tested. Frozen sections were thawed and washed in PBS immediately before the imaging. Using the contact mode imaging of the JPK AFM, several images were captured at each location on each sample. Reduced scan areas were then selected to obtain the structural details of the tissue. MSNL-10 silicon nitride

cantilevers (Bruker, Mannheim, Germany) with a spring constant of 0.01–0.1 N m^{-1} and a nominal tip radius of 2 nm were applied for imaging. The AFM imaging was performed in an ambient environment of 20–25 °C. Biosphere Au reflex (CONT-Au) cantilevers (Nanotools USA LLC, Henderson, NV) with a nominal spring constant of 0.2 N m^{-1} [a 450 μm length, and a nominal resonance frequency of 13 kHz in air] integrated spherical tip of radii 2 μm (±10%) and 5 μm (±10%) were applied for indentation measurements of the bulk tissue immersed in PBS. The AFM probe was navigated over the tissue guided by light microscopy (Figure 1c,d). Super-sharp CONTR cantilevers with diamond-like carbon nanotip of radius 2–3 nm (Nanotools USA LLC, Henderson, NV) [a 450 μm length, and a nominal resonance frequency of 13 kHz in air, and a spring constant of 0.2 N m^{-1}] were used for ultrastructural indentation. All AFM measurements were performed in wet environment with tissue being submerged in PBS. The indentation rate was set to 0.1, 0.5, 1, 2, and 5 μm s^{-1}. Prior to each indentation test, the deflection sensitivity of the AFM cantilever was calibrated by engaging the cantilever on the surface of a clean microscope slide. The precise spring constant of the cantilever was calibrated with the thermal noise fluctuations in air by fitting the first free resonance peak of the AFM cantilever to that of a simple harmonic oscillator using the JPK software.[56] During the indentation, controlled deformation was applied to the tissue sample in hydrated state and the compressive feedback forces were recorded and measured through cantilever deflection (Figure 1d,e).

AFM Indentation: Indentation force F versus displacement δ were recorded to produce F–δ curves by translating cantilever deflection into force F through $F = k\delta$, with k being the cantilever spring constant (Figure 1e). The elastic modulus of the probed samples at each point was obtained by fitting the initial portion (i.e., the contact part) of the approaching part of the force-deflection curves to the standard Hertzian contact model for a spherical indenter of radius R. Using minimum required set points, deformations were set to be infinitesimal and purely elastic with small strain to allow the application of the Hertzian model and further to avoid damaging the tissue microstructure. The tissue was assumed incompressible with Poisson's ratio of 0.5. In the case of soft biological tissues, the elastic modulus E is an accepted measure for the mechanical properties of the tissue only within the small deformation and small strain elastic regime.[57] Five biological replicates, three layers each, with three slides per layer, and two replicate sections per region were indented to measure the elastic modulus at each layer. In each case, over 4×4 points in at least ten different 30 μm $\times$ 30 μm regions in planar sections in each of the three layers of human aorta were indented on each slide, to obtain a minimum of 400 F–δ curves per sample. Force–displacement curves without clear contact point were excluded from the analysis. Single points were repeatedly indented to make sure variation in the elastic modulus as a result of repeated indentation is negligible and no damage is made on the tissue surface. Local variations in the stiffness of each aortic layer at the tissue and subtissue ultrastructural levels were shown in color-coded force maps (Figure 3a–c and 4a–c, respectively). The National Institute of Health ImageJ software and the JPK data processing software were used to analyze the D-banding periodicity and thickness of the collagen fibrils within each image.

Local mechanical properties of a soft tissue as a heterogeneous and anisotropic material were interrogated from its response to the AFM indentation load. To obtain such properties in an accurate way, sample preparation is crucial to preserve the tissue structure pristine and with the least amount of artifacts.[58] As an instance, sample preparation can influence the mechanical properties of the indented sample due to its effect on the roughness of the surface. To minimize the surface roughness, frozen tissue was sectioned with microtome to reach the minimum roughness prior to indentation test. Further, the indentation depth was selected to be much larger than the surface roughness.[45] The contact stiffness of the sample is defined as $dF/d\delta$ with F denoting the indenting force and δ being the resulting indentation depth on the surface of the sample. Indentation modulus of the sample is related to the contact stiffness and is contingent upon the contact area between the AFM tip and the sample. The contact area is usually represented by the contact radius a, and depends on the indentation depth and indentation rate, radius of the indenting sphere and the roughness and elastic response of the sample. Several contact theories have been presented to extract the elastic response of a planar surface indented by a spherical indenter in the absence of plastic deformation. These theories relate the indenting force F to the indentation depth δ and the contact radius a in different ways. Among such theories, the Hertzian contact model,[59] Johnson–Kendall–Roberts (JKR) model,[19,60] and Derjaguin–Muller–Toporov (DMT) model [61] are the most notable. While Hertzian model ignores the adhesion effect between the spherical tip and the sample, the JKR and DMT models account for the adhesion effect between the spherical tip and the sample. Application of all these theories stipulates that the deformation of the sample is purely elastic and infinitesimal compared with the thickness of the sample and the radius of the indenting sphere. For indenting soft samples with large adhesion effect using tips with large radii, JKR model is preferred. However, in case of indenting stiff materials with small adhesion effect using tips with small radii, the DMT model is preferred. Thus, for soft tissues in wet state with large adhesion effects using large spherical tips, JKR model is preferred. In Hertzian contact model,[59] the contact radius a is related to the indenting force F through

$$a = \left(\frac{3RF(1-\nu^2)}{4E}\right)^{1/3} \tag{1}$$

with R being the radius of the spherical tip, and ν and E being the Poisson's ratio and elastic modulus of the sample, respectively. The indentation depth δ is expressed in terms of the contact radius as

$$\delta = \frac{a^2}{R} = \left(\frac{9F^2(1-\nu^2)^2}{16RE^2}\right)^{1/3} \tag{2}$$

Indentation of some biological tissues, plant cells, and similar biological materials in wet state includes adhesion effects between the tip and the sample.[52] This effect is observed in the region with negative force value during unloading.[62] When this effect is significant, the common Hertzian contact mechanics model might overestimate the stiffness of the surface.[63] As such, the JKR model[19] has been shown to be accurate to account for the adhesion effect between the spherical tip and the sample when adhesion forces are considerable in comparison with the indenting load.[64] As noted before, when the adhesion effect between the tissue sample and the indenting sphere (which is shown as the jump-off in the indentation curve) is much smaller than the maximum load, Hertzian model can be applied to extract the sample stiffness. In case adhesion is considerable, the work of adhesion W is calculated from the indentation curve, followed by calculating the contact radius a and then the elastic modulus.[19,64] In view of minimal adhesion effect observed in our curves (see Figure 7 for instance), Hertzian contact model has been utilized in our study.[65,66]

AFM Height and Force Mapping: Representative force maps from regions and subregions in intima, media, and adventitia in the three samples are created by processing the force–displacement curves into height and stiffness maps (see Figure 1f–g and 3 and 4). All force–displacement curves from the AFM measurements are combined within a selected mesh. The extension at which the applying force reaches a certain set point is taken as the intensity at that point. Using a certain set point value, the indentation depth in stiffer regions is smaller due to larger local stiffness, which yields larger probe deflection. In compliant regions however, indentation depth is larger as a result of higher deformation of the sample and thus, the deflection of the probe is smaller. Regions with less indentation depth therefore appear higher than regions with equal height prior to the indentation but more indented due to lower stiffness (see height images in Figure 4). The stiffness maps show the elastic modulus values of the tissue in a respective color scale, with their corresponding elastic modulus distribution histograms. Each pixel in the force maps represents a force curve. This method is sensitive to the initial height and to the stiffness of the tissue under the scanning probe.

Tensile Testing: Quasistatic uniaxial tensile tests were performed on circumferential and longitudinal strips from the media layer of donors I, IV,

and V using a system specifically designed for mechanical characterization of soft tissue.[67] An Interface WMCFP-1000 g load cell was used to measure the force. The strip was immersed in a thermal bath of physiological saline solution (0.9% NaCl in volume) maintained at 37 °C. The tensile force measurement had an accuracy of ±0.01 N. The test was performed at a displacement rate of 0.05 mm s^{-1}. The measured forces were converted to the first Piola–Kirchhoff stresses (i.e., engineering stresses) using the measured cross section of the strip. The distance between the grips was adjusted to achieve an initial load-free position of the strip. An Epsilon ONE-52PT video-extensometer was used to measure the strain at the central portion of the strip.

Statistical Analysis: Data visualization and statistical analysis were performed using GraphPad Prism software (Version 5.03). Statistical differences between layers were assessed using one-way repeated measures analysis of variance with Bonferroni post hoc multiple comparison tests (significance level of 0.05). Data are expressed as mean±standard deviation (SD) throughout the article unless otherwise stated.

Acknowledgements

M.A. acknowledges the NSERC PDF award #516501-2018. M.A. (PI) acknowledges the NSERC Discovery (#533985-18) and NSERC RTI (#2019-00057) grants. N.L. acknowledges FRQNT PDF awards # 256561 and 295553. The authors gratefully acknowledge A. Kassab for the preparation of aortic tissues provided by Transplant Quebec, and GCRC histology core at McGill University for tissue sectioning. M.A. and M.A. (PI) are also grateful to the Collaborative Advanced Microscopy Laboratories (CAMiLoD) at the University of Toronto for the application of their atomic force microscope as an external user.

Conflict of Interest

The authors declare no conflict of interest.

Author Contributions

M.A. and M.A. (PI) conceptualized and designed the study. M.A. performed the experiments, contributed in data analysis and interpreting the results, prepared the figures, and wrote the manuscript. M.A. (PI) supervised the study and contributed in the interpretation of the results, writing and editing. H.D.E. cosupervised the study and contributed in the interpretation of the results, writing and editing. N.L. performed the data analysis and contributed in figure preparation. F.G. contributed in tensile testing and sample handling.

Data Availability Statement

The data that support the findings of this study are available from the corresponding author upon reasonable request.

Keywords

atomic force microscopy, D-spacing, extracellular matrix, fibrillar collagen, force mapping, human aorta, nanoindentation, nanomechanical characterization, tissue ultrastructural analysis

Received: December 20, 2021
Revised: January 7, 2022
Published online: February 10, 2022

[1] W.-C. Yeh, P.-C. Li, Y.-M. Jeng, H.-C. Hsu, P.-L. Kuo, M.-L. Li, P.-M. Yang, P. H. Lee, *Ultrasound Med. Biol.* **2002**, *28*, 467.
[2] M. J. Paszek, N. Zahir, K. R. Johnson, J. N. Lakins, G. I. Rozenberg, A. Gefen, C. A. Reinhart-King, S. S. Margulies, M. Dembo, D. Boettiger, D. A. Hammer, V. M. Weaver, *Cancer Cell* **2005**, *8*, 241.
[3] P. P. Provenzano, D. R. Inman, K. W. Eliceiri, J. G. Knittel, L. Yan, C. T. Rueden, J. G. White, P. J. Keely, *BMC Med.* **2008**, *6*, 1.
[4] A. Samani, D. Plewes, *Phys. Med. Biol.* **2007**, *52*, 1247.
[5] K. Hayashi, K. Ide, T. Matsumoto, *J. Biomech. Eng.* **1994**, *116*, 284.
[6] F. L. Wuyts, V. J. Vanhuyse, G. J. Langewouters, W. F. Decraemer, E. R. Raman, S. Buyle, *Phys. Med. Biol.* **1995**, *40*, 1577.
[7] B. C. Isenberg, P. A. DiMilla, M. Walker, S. Kim, J. Y. Wong, *Biophys. J.* **2009**, *97*, 1313.
[8] N. D. Leipzig, M. S. Shoichet, *Biomaterials* **2009**, *30*, 6867.
[9] A. Subramanian, H-.Y. Lin, *J. Biomed. Mater. Res. A* **2005**, *75*, 742.
[10] N. Latifi, M. Asgari, H. Vali, L. Mongeau, *Sci. Rep.* **2018**, *8*, 1.
[11] C. T. McKee, J. A. Wood, N. M. Shah, M. E. Fischer, C. M. Reilly, C. J. Murphy, P. Russell, *Biomaterials* **2011**, *32*, 2417.
[12] J. S. Bredfeldt, Y. Liu, M. W. Conklin, P. J. Keely, T. R. Mackie, K. W. Eliceiri, *J. Pathol. Inform.* **2014**, *5*, 28.
[13] M. Asgari, N. Latifi, H. K. Heris, H. Vali, L. Mongeau, *Sci. Rep.* **2017**, *7*, 1.
[14] G. Binnig, C. F. Quate, C. Gerber, *Phys. Rev. Lett.* **1986**, *56*, 930.
[15] C. A. Grant, P. C. Twigg, D. J. Tobin, *Acta Biomater.* **2012**, *8*, 4123.
[16] T. Luque, E. Melo, E. Garreta, J. Cortiellae, J. Nichols, R. Farré, D. Navajas, *Acta Biomater.* **2013**, *9*, 6852.
[17] C. T. McKee, J. A. Last, P. Russell, C. J. Murphy, *Tissue Eng. Part B Rev.* **2011**, *17*, 155.
[18] Y. Zhu, Z. Dong, U. C. Wejinya, S. Jin, K. Ye, *J. Biomech.* **2011**, *44*, 2356.
[19] K. L. Johnson, *Contact Mechanics*, Cambridge University Press, Cambridge, UK **1987**.
[20] S. Sherifova, G. A. Holzapfel, *Acta Biomater.* **2019**, *99*, 1.
[21] M. Amabili, P. Balasubramanian, I. Bozzo, I. D. Breslavsky, G. Ferrari, *J. Mech. Behav. Biomed. Mater.* **2019**, *99*, 27.
[22] M. Amabili, P. Balasubramanian, I. Bozzo, I. D. Breslavsky, G. Ferrari, G. Franchini, F. Giovanniello, C. Pogue, *Phys. Rev. X* **2020**, *10*, 011015.
[23] M. Amabili, G. O. Arena, P. Balasubramanian, I. D. Breslavsky, R. Cartier, G. Ferrari, G. A. Holzapfel, A. Kassab, R. Mongrain, *J. Biomech. Eng.* **2020**, *110*, 109978.
[24] G. Franchini, I. D. Breslavsky, G. A. Holzapfel, M. Amabili, *Acta Biomater.* **2021**, *130*, 291.
[25] M. Amabili, M. Asgari, I. D. Breslavsky, G. Franchini, F. Giovanniello, G. A. Holzapfel, *Acta Biomater.* **2021**, *134*, 401.
[26] J. A. Niestrawska, C. Viertler, P. Regitnig, T. U. Cohnert, G. Sommer, G. A. Holzapfel, *J. R. Soc. Interface* **2016**, *13*, 20160620.
[27] T. C. Gasser, R. W. Ogden, G. A. Holzapfel, *J. R. Soc. Interface* **2006**, *3*, 15.
[28] J. D. Humphrey, G. A. Holzapfel, *J. Biomech.* **2012**, *45*, 805.
[29] A. Berquand, A. Wahart, A. Henry, L. Gorisse, P. Maurice, S. Blaise, B. Romier-Crouzet, C. Pietrement, A. Bennasroune, H. Sartelet, S. Jaisson, P. Gillery, L. Martiny, F. Touré, L. Duca, M. Molinari, *Nanoscale* **2021**, *13*, 1124.
[30] S. Brody, T. Anilkumar, S. Liliensiek, J. A. Last, C. J. Murphy, A. Pandit, *Tissue Eng.* **2006**, *12*, 413.
[31] J. Peloquin, J. Huynh, R. M. Williams, C. A. Reinhart-King, *J. Biomech.* **2011**, *44*, 815.
[32] P. Tracqui, A. Broisat, J. Toczek, N. Mesnier, J. Ohayon, L. Riou, *J. Struct. Biol.* **2011**, *174*, 115.
[33] A. Rezvani-Sharif, M. Tafazzoli-Shadpour, A. Avolio, *Cardiovasc. Eng. Technol.* **2019**, *10*, 181.

[34] B. Jones, J. R. Tonniges, A. Debski, B. Albert, D. A. Yeung, N. Gadde, A. Mahajan, N. Sharma, E. P. Calomeni, M. R. Go, C. P. Hans, G. Agarwal, *Acta Biomater.* **2020**, *110*, 129.
[35] H. Qiu, Y. Zhu, Z. Sun, J. P. Trzeciakowski, M. Gansner, C. Depre, R. R. G. Resuello, F. F. Natividad, W. C. Hunter, G. M. Genin, E. L. Elson, D. E. Vatner, G. A. Meininger, S. F. Vatner, *Circ. Res.* **2010**, *107*, 615.
[36] D. Sicard, L. E. Fredenburgh, D. J. Tschumperlin, *J. Mech. Behav. Biomed. Mater.* **2017**, *74*, 118.
[37] J. R. Tonniges, B. Albert, E. P. Calomeni, S. Roy, J. Lee, X. Mo, S. E. Cole, G. Agarwal, *Microsc. Microanal.* **2016**, *22*, 599.
[38] P. Fratzl, *Collagen: Structure and mechanics, an introduction*, Springer, New York **2008**.
[39] M. J. Buehler, *Proc. Natl. Acad. Sci. U.S.A.* **2006**, *103*, 12285.
[40] M. Fang, E. L. Goldstein, A. S. Turner, C. M. Les, B. G. Orr, G. J. Fisher, K. B. Welch, E. D. Rothman, M. M. Banaszak Holl, *ACS Nano* **2012**, *6*, 9503.
[41] K. P. Dingemans, P. Teeling, J. H. Lagendijk, A. E. Becker, *Anat.* **2000**, *258*, 1.
[42] A. Gautieri, S. Vesentini, A. Redaelli, M. J. Buehler, *Matrix Biol.* **2012**, *31*, 141.
[43] J. H. N. Lindeman, B. A. Ashcroft, J.-W. M. Beenakker, M. Van Es, N. B. R. Koekkoek, F. A. Prins, J. F. Tielemans, H. Abdul-Hussien, R. A. Bank, T. H. Oosterkamp, *Proc. Natl. Acad. Sci. U.S.A.* **2010**, *107*, 862.
[44] S. L. Chang, P. S. Howard, H. P. Koo, E. J. Macarak, *Neurourol. Urodyn.* **1998**, *17*, 135.
[45] M. Asgari, J. Abi-Rafeh, G. N. Hendy, D. Pasini, *J. Mech. Behav. Biomed. Mater.* **2019**, *93*, 81.
[46] V. F. Achterberg, L. Buscemi, H. Diekmann, J. Smith-Clerc, H. Schwengler, J. Meister, H. Wenck, S. Gallinat, B. Hinz, *J. Investig. Dermatol.* **2014**, *134*, 1862.
[47] C. F. Guimarães, L. Gasperini, A. P. Marques, R. L. Reis, *Nat. Rev. Mater.* **2020**, *5*, 351.
[48] R. E. Shadwick, *J. Exp. Biol.* **1999**, *202*, 3305.
[49] Z. Liu, M. A. Meyers, Z. Zhang, R. O. Ritchie, *Prog. Mater. Sci.* **2017**, *88*, 467.
[50] J. Ren, Y. Wang, Y. Yao, Y. Wang, X. Fei, P. Qi, S. Lin, D. L. Kaplan, M. J. Buehler, S. Ling, *Chem. Rev.* **2019**, *119*, 12279.
[51] M. Asgari, N. A. Alderete, Z. Lin, R. Benavides, H. D. Espinosa, *Acta Biomater.* **2021**, *122*, 236.
[52] M. Asgari, V. Brulé, T. L. Western, D. Pasini, *Sci. Rep.* **2020**, *10*, 506.
[53] V. Brulé, A. Rafsanjani, M. Asgari, T. L. Western, D. Pasini, *J. R. Soc. Interfaces* **2019**, *16*, 454.
[54] I. D. Medalsy, D. J. Müller, *ACS Nano* **2013**, *7*, 2642.
[55] H. D. Espinosa, J. E. Rim, F. Barthelat, M. J. Buehler, *Prog. Mater. Sci.* **2009**, *54*, 1059.
[56] J. L. Hutter, J. Bechhoefer, *Rev. Sci. Instrum.* **1993**, *64*, 1868.
[57] A. J. Engler, F. Rehfeldt, S. Sen, D. E. Discher, *Methods Cell Biol.* **2007**, *83*, 521.
[58] S. P. Ho, H. Goodis, M. Balooch, G. Nonomura, S. J. Marshall, G. Marshall, *Biomaterials* **2004**, *25*, 4847.
[59] H. Hertz, *Ueber Die Berhrung Fester Elastischer Krper*, De Gruyter, Berlin **2021**, pp. 156.
[60] K. L. Johnson, K. Kendall, A. Roberts, *Proc. R. Soc. Lond.* **1971**, *324*, 301.
[61] B. V. Derjaguin, V. M. Muller, Y. P. Toporov, *J. Colloid Interface Sci.* **1975**, *53*, 314.
[62] H. J. Butt, B. Cappella, M. Kappl, *Surf. Sci. Rep.* **2005**, *59*, 1.
[63] F. Carrillo, S. Gupta, M. Balooch, S. J. Marshall, G. W. Marshall, L. Pruitt, C. M. Puttlitz, *J. Mater. Res.* **2005**, *20*, 2820.
[64] D. M. Ebenstein, K. J. Wahl, *J. Colloid Interface Sci.* **2006**, *298*, 652.
[65] R. Garcia, *Chem. Soc. Rev.* **2020**, *49*, 5850.
[66] A. Viljoen, M. Mathelié-Guinlet, A. Ray, N. Strohmeyer, Y. J. Oh, P. Hinterdorfer, D. J. Müller, D. Alsteens, Y. F. Dufrêne, *Nat. Rev. Dis. Primers* **2021**, *1*, 1.
[67] G. Franchini, I. D. Breslavsky, F. Giovanniello, A. Kassab, G. A. Holzapfel, M. Amabili, *Proc. Natl. Acad. Sci. U.S.A.* **2022**, *119*, e2117232119.